An investigation of the energy storage properties of a 2D α-MoO_3-SWCNTs composite films

Beatriz Mendoza-Sánchez[a,*], Damien Hanlon[b], João Coelho[a], Sean O' Brien[b], Henrik Pettersson[b], Jonathan Coleman[c], and Valeria Nicolosi[d,*]

[a] *Trinity College Dublin, School of Chemistry and CRANN, Dublin 2, Ireland*
[b] *Trinity College Dublin, School of Physics, Dublin 2, Ireland*
[c] *Trinity College Dublin, School of Physics, CRANN and AMBER, Dublin 2, Ireland*
[d] *Trinity College Dublin, Schools of Chemistry, Physics, CRANN and AMBER, Dublin 2, Ireland*

Abstract

2D α-MoO_3 was synthesized using a facile, inexpensive and scalable liquid-phase exfoliation method. 2D α-MoO_3/SWCNT (85 wt%/15 wt%) composite films were manufactured by vacuum filtration and their energy storage properties were investigated in a $LiClO_4$/propylene carbonate electrolyte in a 1.5 V to 3.5 V vs. Li^+/Li electrochemical window. Cyclic voltammetry showed typical ion intercalation peaks of α-MoO_3 and a capacitance of 200 F g^{-1} was achieved at 10 mV s^{-1} and 82 F g^{-1} at 50 mV s^{-1}. The composite electrodes achieved a capacitive charge storage of 375 C g^{-1} and a diffusion-controlled maximum charge storage of 703 C g^{-1}. The latter being superior to the charge storage achieved by previously reported mesoporous α-MoO_3, produced using more cumbersome multi-step templating methods, and α-MoO_3 nanobelts . This superior Li-ion intercalation charge storage

*Corresponding authors
Email addresses: beatrix.mendoza@gmail.com (Beatriz Mendoza-Sánchez), nicolov@tcd.ie (and Valeria Nicolosi)

was attributed to the shorter ion-transport paths of 2D α-MoO_3 as compared to other nanostructures. Galvanostatic charge-discharge experiments showed a maximum charge storage of 123.0 mAh g^{-1} at a current density of 100 mA g^{-1}.

Keywords:
2D α-MoO_3, single-walled carbon nanotubes, energy storage, Li-ion intercalation

---

1. Introduction

Due to its properties, α-MoO_3 is an attractive material for energy storage applications. Firstly, α-MoO_3 has a layered crystal structure suitable for ion intercalation. Each layer of the 2D-layered structure of orthorhombic α-MoO_3 is composed of two octahedron nets that share O-O edges along the [001] direction and corners along the [100] direction, and each layer is linked to an adjacent layer by van der Waals forces along the [010] direction [1, 2]. Secondly, due to the high oxidation state of the metal (Mo^{6+}) in α-MoO_3, this material has high open circuit potential, and thus, it is capable of high energy storage when tested in a typical battery set up [3]. Thirdly, due to the various oxidation states of Mo (Mo^{6+}, Mo^{5+}, Mo^{4+}, Mo^{3+}), α-MoO_3 can store energy by undergoing redox activity [4, 5]. α-MoO_3 has mainly been investigated as a battery cathode[3, 6–8] and anode [9, 10] and a high charge storage has been reported. However, drawbacks preventing its application include: characteristic slow kinetics, high irreversibility and poor cycle stability. More recently, α-MoO_3 has been investigated as a supercapacitor electrode in a Li-ion based electrolyte and a high charge storage attributed to pseudocapacitive

activity was reported [11]. However, the study did not include cycle stability assessment.

In order to improve charge storage capacity, α-MoO_3 has been nanostructured and combined with carbon-based materials. The literature reports various α-MoO_3 nanostructures including nanoparticles, nanowires and mesoporous nanostructures [9–11] with high surface areas and/or porosity that enables a greater charge storage than their micro-sized counterparts. Due to its semiconducting nature, α-MoO_3 stores charge poorly unless it is provided with an electrically conducting additive. Carbon-based materials such as carbon nanotubes and carbon black are added as conductive additives [9, 12]. Upon repeated Li-ion intercalation de-intercalation, α-MoO_3 expands and contracts eventually causing particle pulverization and loss of particle-particle contact [13]. This leads to capacity fading upon cycling. Carbon-based additives not only provide suitable electrical conductivity but also are used to alleviate this pulverization effect serving as a "mechanical buffer" of α-MoO_3 particles[13, 14]. Carbon nanotubes, for example, form nets that buffer volume changes during cycling [12].

2D nanomaterials are typically obtained from layered van der Waals solids that have strong ionic or covalent in-plane bonds that form layers but weak out-of-plane van der Waals bonds [15, 16]. The term "exfoliation" refers to the delamination of layered van der Waals solids by overcoming the van der Waals forces by either shearing parallel or expanding normal to the in-plane direction [15, 16]. Liquid-phase exfoliation utilizes ultrasonic energy and liquid-mediated stabilization to delaminate layered van der Waals solids, resulting in exfoliated nanosheets (the term nano refers to the magnitude of

the thickness) [17, 18]. Liquids, including water and organic solvents, with the correct surface energy or solubility parameters bind by van der Waals interactions to the exfoliated nanosheets with strengths that are similar to the inter-nanosheet binding strength, preventing re-aggregation and reducing the net energy cost of exfoliation [19–21]. In the ideal case, the nanosheets are comprised of a single constituent layer of the original layered solid; however, in practice, the nanosheets consist of few (≈ 10) stacked layers [17].

2D nanomaterials produced by liquid-phase exfoliation offer some scope for application in batteries and supercapacitors due to: (1) high surface area with a typical width of 50 nm, length $<$ 1000 nm, and thickness $<$ 2 - 5 nm [18, 22] (2) high packing density that allows volume reduction of devices, highly relevant in the power electronics industry where miniaturization is important, (3) redox and/or ion-intercalation activity, (4) cost-effectiveness, simplicity and scalability of the liquid-phase exfoliation method, (5) production of the 2D nanomaterials in suspension which allows immediate processability into films using scalable methods such as spray-deposition [23, 24] and ink-jet printing.

In this work, commercially available bulk layered α-MoO_3 was exfoliated in isopropanol resulting in α-MoO_3 nanosheets (2D α-MoO_3) of 400 nm length x 100 nm width x 21 nm thickness. Characterization of the 2D α-MoO_3 has been addressed elsewhere [25]. The 2D α-MoO_3 were combined with single-walled carbon nanotubes (SWCNTs) (85 wt%/15 wt% ratio) in composite film electrodes and their energy storage properties were investigated in a $LiClO_4$/propylene carbonate electrolyte in a 1.5 V to 3.5 V vs. Li^+/Li electrochemical window. The composite electrodes achieved a higher

Li-ion intercalation charge storage (703 C g^{-1}) than other nanostructures, a maximum capacitance of 200 F g^{-1} at 10 mV s^{-1}, and a capacity of 123.0 mAh g^{-1} at a current density of 100 mA g^{-1}.

2. Experimental

2.1. Materials

Single-walled carbon nanotubes (SWCNTs) functionalized with 1-3 wt% carboxylic groups ("P3-SWNT") were supplied by *Carbon Solutions Inc (USA)*; MoO_3 powder (99.98 %, CAS 1313-27-5), isopropanol (IPA 99.9 %), Li wire ($\geq$ 98 % in mineral oil), n-hexane (anhydrous 95 %), lithium perchlorate (battery grade 99.99 %), and propylene carbonate (anhydrous 99.7 %) were supplied by *Sigma Aldrich (Ireland)*; poly (ethyleneimine) (PEI, Mw= 70,000) was supplied by *Alfa-Aesar (UK)*; aluminium foil of 0.025 mm thickness (temper hard Al000420) was supplied by *GoodFellow (UK)*; alumina membrane filters (Anodisc 47, 0.02 μm pore size, Whatman) and nitrocellulose membrane filters (0.02 μm pore size, 10 mm diameter, Millipore) were supplied by *Fisher (Ireland)*.

2.2. Preparation of 2D α-MoO_3 dispersion

A dispersion of 2D α-MoO_3 in IPA was first prepared by liquid-phase exfoliation. MoO_3 powder (30 g) was added to IPA (100 mL) in a 140 ml open top, flat bottomed beaker. The mix was ultrasonicated for 5 hours in a *VCX-750* sonic dismembrator (25 % amplitude and operated under pulsation mode, 9 s on and 2 s off). The beaker was connected to an external cooling system (circulator refrigerated bath) that maintained water at 5 °C circulating around the beaker during ultrasonication. The resulting dispersion was

then centrifuged at 1,500 rpm (RCF = 240) for 110 min. A dispersion of 2D α-MoO_3 in IPA was finally obtained by collecting the supernatant (top 75 %) using a volumetric pipette. The concentration of the 2D α-MoO_3 dispersion (0.17 mg ml^{-1}) was determined by weighing before and after vacuum filtration onto an alumina membrane filter (pore size 0.02 μm).

2.3. Preparation of 2D α-MoO_3/SWCNT composite dispersion

A dispersion of 2D α-MoO_3 in IPA was prepared as described above. SWCNTs (5 mg) were dispersed in IPA (50 mL) at a concentration of 0.1 mg ml^{-1}. This suspension was then ultrasonicated for 30 min in a *VCX-750* sonic dismembrator (40 % amplitude) while cooling down, then ultrasonicated for one hour in a *ElmasonicP120H* sonic bath (37 kHz, 60 % power) followed by an additional 30 min in the *VCX-750* sonic dismembrator. This dispersion was then mixed without centrifugation with a 2D-MoO_3/IPA dispersion of predetermined concentration to form a composite of known SWCNTs wt %.

2.4. Electrode manufacture

The 2D α-MoO_3/SWCNT composite dispersion was vacuum filtrated using a nitrocellulose membrane filter and dried at room temperature. These films were subsequently transferred onto aluminum foil substrates (pre-coated by spray deposition with a $\approx$ 5 nm layer of 0.1 % wt/wt PEI solution in water) using the transfer method of Wu et al.[26]. The electrodes were then cut into 18 mm discs. The average mass and thickness of the 2D-MoO_3-SWCNT composite electrodes were 0.7 mg and 1 μm respectively. Electrodes of solely 2D α-MoO_3 were manufactured following the same procedure.

Equipment and characterization techniques. Transmission electron microscopy (TEM) images were obtained using a *FEI-Titan* operated at 300 keV; scanning electron microscopy (SEM) images were obtained using a *Carl Zeiss Ultra Plus* operated at an acceleration voltage of 5 kV; Raman (RS) spectra were recorded at room temperature using a *Witec Alpha 300* system with a laser excitation wavelength of 532 nm. Laser power of $\approx$ 0.4 mW was used with a 20x objective lens. Spectra were acquired for each sample by averaging 25 distinct spectra, each with an acquisition time of 30 s; Spray deposition of PEI on substrates was performed using a *USI Prism Ultracoat 300* spray deposition equipment; ultrasonication was performed in a *VCX-750 (VibraCell)* sonic dismembrator with a 0.5 inch probe (maximum delivery power of 750 W and operating frequency of 20 kHz), and an *ElmasonicP120H (Fisher FB11207)* sonic bath (effective power of 330 W and 37/80 kHz operating frequency); cooling during ultrasonication was performed with a circulator *Isouk 4100 R20* refrigerated bath (Fisher FB60818); centrifugation was performed in a *Hettich Mikro 220R* centrifuge with a fixed angle rotor 1060. The rotational speed ω (rpm) and the relative centrifugal force (non-dimensional, relative to g = 9.8 m s^{-2}) are both quoted and related by RCF = 106.4 x $10^{-6}\omega^2$; electrode thickness was determined by step height measurements in a *Dektak 6M* profilometer (*Veeco Instruments, Inc*) and the weight of deposited films was measured using a *Sartorius Ultramicrobalance MSE-2.7S-000-DF* with a 0.0001 mg readability; the surface area of the 2D α-MoO_3 was determined with a *Autosorb iQ (Quantachrome)* gas sorption analyzer to read nitrogen adsorption isotherms and using the Brunauer-Emmett-Teller (BET) method; electrochemical mea-

surements were performed with a *Reference 600/EIS300 Gamry* potentiostat/galvanostat; the electrodes were tested in a three-electrode configuration using an *ECC-Combi (EL-CELL, Germany)* battery test cell. The cell assembly was performed in a *MB-Unilab (1200/780) (MBRAUN, Germany)* glove box workstation; electrical conductivity was calculated using a four probe method with a Keithley 2400 source metre. Silver contacts were used with spacings of about 1 mm.

Electrochemical characterization. 2D α-MoO_3/SWCNT electrodes were tested in a three-electrode electrochemical cell configuration using a *Reference 600/EIS300 Gamry* potentiostat/galvanostat; Li wire and Li ribbon as reference and counter electrodes, respectively; glass fibre separators (1.55 mm thickness, 18 mm diameter); and 1 M $LiClO_4$ in propylene carbonate as the electrolyte. The cells were assembled in a glove box workstation maintaining H_2O and O_2 levels below 0.1 ppm. The electrodes were dried in vacuum (100 °C for 1 hour) prior to the electrochemical tests and the Li wire was freed of protective mineral oil by extensive rinsing with n-hexane. Cyclic voltammetry experiments and galvanostatic charge-discharge experiments were performed in a potential range of 1.5 to 3.5 V vs. Li/Li^+.

3. Results and discussion

3.1. Characterization of Materials

Characterization of the 2D α-MoO_3 by TEM, SEM and Raman were reported in our previous work [25]. Here we describe some aspects relevant to the energy storage application of 2D α-MoO_3. As shown in Figure 1a, the starting material consisted of microsized platelets. Figure 1d shows TEM mi-

crographs of the liquid-phase exfoliated 2D α-MoO_3 with typical dimensions of 400 nm length x 100 nm width x 21 nm thickness (mean size determined by atomic force microscopy measurements over 100 nanosheets) [25]. The high-resolution TEM (HRTEM) image in Figure 1e show the high structural quality of the as synthesized nanoshets. The fast Fourier transform (FFT) (inset of Figure 1e) shows that the lattice spacings correspond to the alpha phase of MoO_3. The viewing direction of the HRTEM image (see scheme in Figure 1f) is along the [010] zone axis. The (010) planes are shown with lattice spacings of 0.36 nm along the [001] direction (edge sharing along the c axis, i.e. the nanosheet width) and 0.38 nm along the [100] direction (corner sharing along the a axis, i.e. the nanosheet length).

Raman spectroscopy was performed on the powder of the starting material (SEM image shown in Figure 1a) and on a thin film (SEM image shown in Figure 1b) of as-synthesized material. Figure 1c shows the Raman spectra (excitation wavelength of 532 nm) of both samples. Both spectra showed characteristic bands of the orthorhombic phase of MoO_3 [27–29]: 996 cm^{-1}, 820 cm^{-1}, 666-667 cm^{-1}, 480 cm^{-1}, 380 cm^{-1}, 366 cm^{-1}, 338 cm^{-1}, 291 cm^{-1}, 285 cm^{-1}, 245 cm^{-1}, 217 cm^{-1}, 197 cm^{-1}, and 158 cm^{-1}. The stoichiometry of the samples was determined by following the methodology of Dieterle et al. where the ratio of intensities of the band at 285 cm^{-1} to that at 295 cm^{-1} is correlated to the stoichiometry [27]. Here the latter band was shifted to 291 cm^{-1}, indicating the presence of oxygen vacancies. Applying this analysis, the stoichiometry of starting material and exfoliated material were determined as $MoO_{2.96}$ and $MoO_{2.95}$ respectively [25]. Therefore, a negligible amount of oxygen vacancies were introduced by the exfoliation procedures.

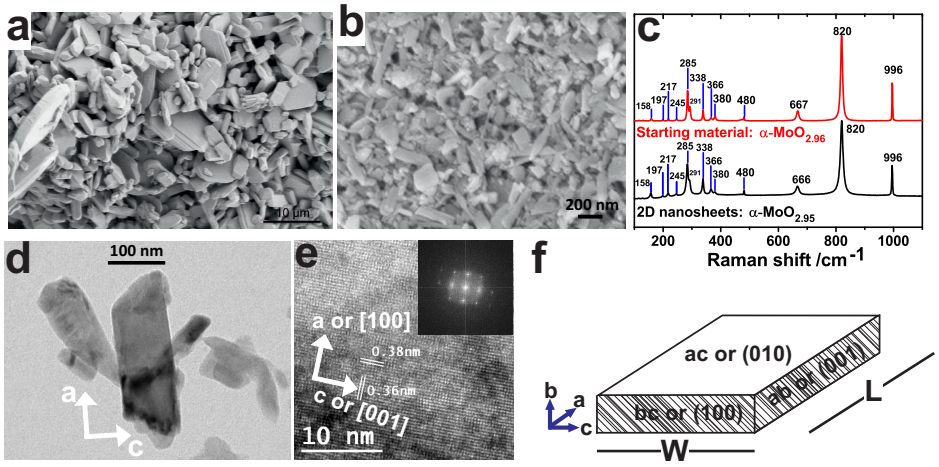

Figure 1: (a) SEM image of MoO_3 starting material, (b) SEM image of a film of α-MoO_3 nanosheets produced by vacuum filtration, (c) Raman spectra of raw material MoO_3 and a film of exfoliated α-MoO_3 nanosheets where the text indicates specific Raman shifts (cm^{-1}), (d) TEM and (e) HRTEM micrographs and corresponding fast Fourier transform (inset) of a representative α-MoO_3 nanosheet where the arrows indicate the a ([100]) and c ([001]) lattice directions and the text indicates lattice spacings, (f) scheme describing a nanosheet geometry and planes.

For practical reasons, we will refer to the exfoliated material as 2D α-MoO_3.

3.2. Electrochemical characterization

The charge storage properties of 2D α-MoO_3 were investigated in a 1 M $LiClO_4$/propylene carbonate electrolyte in a half cell configuration using Li foil as reference and counter electrodes. Due to is semiconducting nature, α-MoO_3 can store charge only if provided with an electrically conductive additive [7, 30]. In our previous work, a study was conducted to optimize the weight percentage of SWCNTs in a 2D α-MoO_3/SWCNT composite that results in maximum capacitance. Investigation by cyclic voltammetry (CV)

(at 10 mV s^{-1}) showed that the capacitance increased dramatically from 2 F g^{-1} to 156 F g^{-1} (Figure 2a) when the f_{SWCNT} increased from 0-2.5 wt% to a critical mass fraction $f^{C}_{SWCNT} = 5$ wt%. The capacitance increased slightly to 200 F g^{-1} for a $f_{SWCNT} = 15$ wt% with no further increase upon further increase of SWCNT mass fraction. As shown in Figure 2b, the same behaviour held for a span of scan rates from 0.1 to 100 mV s^{-1}. In these studies the capacitance was determined considering the total charge storage per unit mass of electrode.

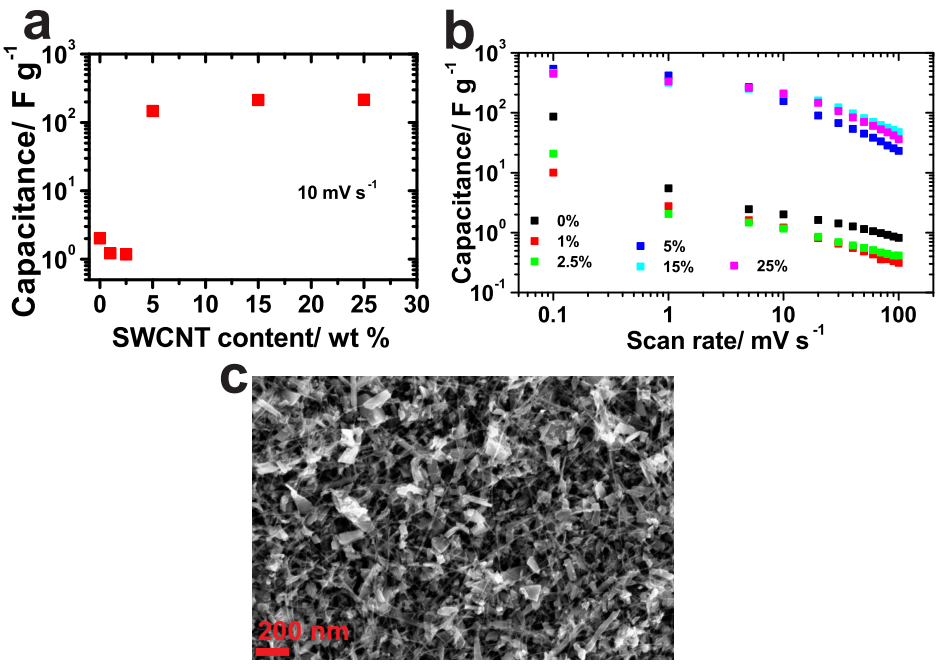

Figure 2: (a), (b) specific capacitance of 2D α-MoO_3/SWCNT electrode films versus mass fraction of SWCNTs as determined by cyclic voltammetry at (a) 10 mv s^{-1} and (b) 0.1 mv s^{-1} to 100 mv s^{-1} scan rate, and (c) SEM image of a 2D α-MoO_3/SWCNT (85 wt%/ 15wt %) film.

Subsequent testing was performed on electrodes with a 15 wt% SWCNT

content. The SEM image in Figure 2c shows the surface of 2D α-MoO_3/SWCNT (85 wt%/ 15 wt%) composite electrode, where a high degree of interleaving of the SWCNTs in between and around the MoO_3 nanosheets had been achieved, not only developing an electrically conducting network, but also providing a degree of mesoporosity desirable to facilitate electrolyte accessibility [12].

The ion intercalation events in the 2D α-MoO_3/SWCNT (85 wt%/ 15wt %) composite electrodes were studied by CV at a scan rate of 0.1 mV s^{-1}. As shown in Figure 3a, a series of well-defined anodic (a) and cathodic peaks (c) were identified. The identified cathodic peaks were: c_1 (2.78 V), c_2 (2.50 V), c_3 (2.34 V), $c_{4,S}$ (2.25 V), and c_5 (2.10 V) (S indicates a shoulder), and the identified anodic peaks were: a_1 (2.9 V), $a_{1,S}$ (3.02 V), a_2 (2.67 V, only first cycle), a_3 (2.36 V), and $a_{3,S}$ (2.44 V). As previously reported in the literature, most of the peaks are associated to Li-ion intercalation events characteristic of the orthorhombic phase of MoO_3 [4, 11, 31, 32]: (1) the cathodic peak c_1 has been associated to an irreversible phase transformation involving a crystal lattice expansion [4, 11, 31, 32], and (2) the couples (c_2, a_2) and (c_3, a_3) have been associated to intra- and inter-layer Li-ion intercalation events into the orthorhombic crystal structure of α-MoO3 [4, 11, 31, 32]. Here, some peaks not previously described in the literature, $c_{4,S}$ (2.25 V), and c_5 (2.10 V), were identified and they may be associated to ion intercalation events that might have been enabled by the 2D nature of the 2D α-MoO_3 nanosheets. As shown in Figure 3a, most peaks are irreversible and only present up to the first cycle (e.g. a_2) and third cycle (e.g $c_{4,S}$). As shown in Figure 3b, at larger scan rates only the peaks c_3, a_3 - and to some degree a_1

- remained electrochemically active describing a reversible inter-layer Li-ion intercalation.

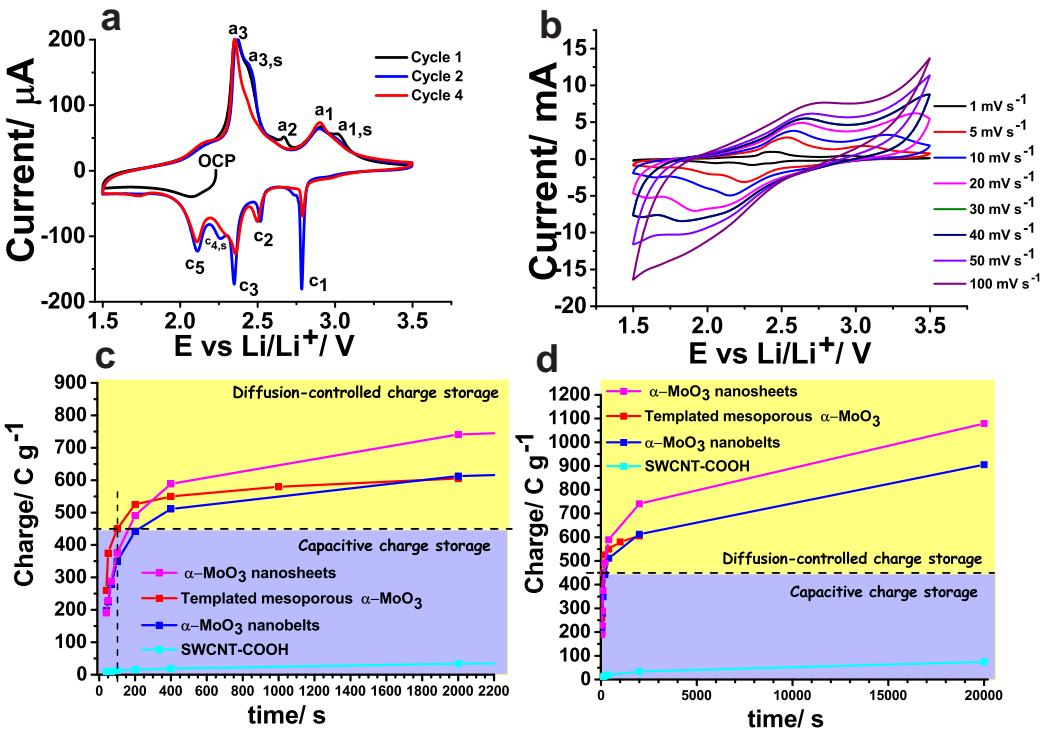

Figure 3: Charge storage performance of 2D α-MoO_3/SWCNT (85 wt%/ 15 wt%) electrodes evaluated by cyclic voltammetry in a half cell configuration vs Li/Li^+ in 1 M $LiClO_4$/PC electrolyte: (a) cyclic voltammograms at 0.1 mV s^{-1} scan rate, (b) cyclic voltammograms at 10 mV s^{-1} to 100 mV s^{-1} scan rate, (c) and (d) charge stored by individual components 2D α-MoO_3 and SWCNTs of the composite electrode per unit mass of the single component versus charging time $t = \Delta V/\nu_s$ where ΔV is the electrochemical window and ν_s is the scan rate. Other data lines are added for comparison versus other α-MoO_3 nanostructures reported in the literature: α-MoO_3 nanobelts [12] and mesoporous templated α-MoO_3 [11].

α-MoO_3 stores energy by three mechanisms: double layer capacitance, redox pseudocapacitance, and diffusion controlled Li-ion intercalation [11].

The first two mechanisms are fast whereas ion intercalation is slower due to diffusion control. Capacitive contributions to charge storage can be considered to occur at a 20-100 s time scale (100 mV s^{-1} to 20 mV s^{-1} CV scan rate) [11]. Charge storage contributions controlled by diffusion, i.e. ion intercalation, can be considered to occur at a 100-20,000 s time scale (20 mV s^{-1} to 0.1 mV s^{-1} CV scan rate) [11]. Figures 3c and 3d show the charge storage capacity of 2D α-MoO_3 (charge of the 2D α-MoO_3 component in a composite electrode per unit mass of 2D α-MoO_3) as a function of charging time, as determined by CV. For a given charging time, the overall charge storage is the sum of the capacitive plus the diffusion controlled contributions. For times shorter than 100 s (to the left of the vertical dotted line) there is only a capacitive contribution.

The performance of 2D α-MoO_3 was compared to the performance of previously reported α-MoO_3 nanobelts [12] and templated mesoporous α-MoO_3 [11]. The capacitive contribution to the charge storage capacity of 2D α-MoO_3 was 375 C g^{-1} (100 s charging time), which was larger than that of α-MoO_3 nanobelts (349 C g^{-1}) and smaller than that of templated mesoporous α-MoO_3 (450 C g^{-1}). The different BET surface areas of the various nanostructures considered (13.7 m^2 g^{-1} for nanobelts $<$ 34.3 m^2 g^{-1} for nanosheets $<$ 200 m^2 g^{-1} for mesoporous α-MoO_3) may explain the difference on the capacitive contribution to energy storage. The charge storage capacity of 2D α-MoO_3 due to diffusion controlled processes was 703 C g^{-1} (20,000 s), 365 C g^{-1} (2,000 s), 213 C g^{-1} (400 s) and 115 C g^{-1} (200 s). As shown in Figures 3c and 3d (yellow area of the plot), these values are much higher than those of α-MoO_3 nanobelts (e.g. 263 C g^{-1} at 2,000 s charging

time) and templated mesoporous α-MoO_3 (e.g. 155 C g^{-1} at 2,000 s charging time). This effect can be attributed to: (1) shorter transport paths of 2D α-MoO_3 (400 nm length x 100 nm width) as compared to α-MoO_3 nanobelts (300-400 nm width and 8-18 μm length) for Li-ions to intercalate between van der Waals gaps (approximately 29 gaps for a 21 nm thick nanosheet if the lattice spacing is b = 1.38 nm) accessed through the ab and bc planes of the nanosheets (Figure 1f) exposed to the electrolyte, and (2) the role of the SWCNTS providing an electrically conducting network and creating a degree of mesoporosity throughout the electrode, thereby facilitating electrolyte access. As shown in Figures 3c and 3d, the charge storage contribution of SWCNTs to the total electrode charge storage was negligible accounting for a maximum of 2.5 %.

The capacitive performance as a function of CV scan rate was investigated. Figure 3b shows the CVs at the different scan rates and Figure 2b shows that the 2D α-MoO_3/SWCNT (85 wt%/ 15 wt%) composite electrodes achieved a capacitance of 200 F g^{-1} at a scan rate of 10 mV s^{-1} (200 s) and was maintained at 82 F g^{-1} at a scan rate of 50 mV s^{-1}. This performance is comparable to that achieved by other pseudocapacitive systems including iron oxides and manganese oxides [33–36].

The cycling stability of the 2D α-MoO_3/SWCNT (85 wt%/ 15 wt%) composite electrode was investigated by galvanostatic charge-discharge curves at a current rate of 100 mA g^{-1} (0.017 mA cm^{-2} for an electrode of 2.54 cm^2). A discharge capacity of 123.0 mAh g^{-1} was achieved during the first cycle. The capacitance retention over 200 cycles was 62%.

4. Conclusions

2D α-MoO_3 was synthesized by liquid-phase exfoliation. 2D α-MoO_3/SWCNT (85 wt%/ 15 wt%) composite electrodes were manufactured and their charge storage properties were investigated. Cyclic voltammetry showed typical ion intercalation peaks of α-MoO_3, and a capacitance of 200 F g^{-1} was achieved at 10 mV s^{-1} and 82 F g^{-1} at 50 mV s^{-1}. The composite electrodes achieved a capacitive charge storage of 375 C g^{-1} and a diffusion-controlled maximum charge storage of 703 C g^{-1}. The latter being superior to the charge storage achieved by α-MoO_3 nanobelts (263 C g^{-1}) and mesoporous α-MoO_3 (155 C g^{-1}). This superior charge storage due to Li-ion intercalation was attributed to shorter ion-transport paths in 2D α-MoO_3 as compared to α-MoO_3 nanobelts. Galvanostatic charge-discharge experiments showed a maximum charge storage of 123.0 mAh g^{-1} at a current density of 100 mA g^{-1}. We can conclude that 2D α-MoO_3 achieved considerable charge storage in the long time regime (100 s-20,000 s) offering potential for applications in batteries. However, this is contingent on improving cycling stability. The capacitive charge storage was superior to that of α-MoO_3 nanobelts and comparable to the performance of other metal oxide nanostructures. Liquid-phase exfoliation is a method to produce active materials that offers clear advantages of cost-effectiveness, ease of processing, and scalability over more cumbersome and expensive templating and hydrothermal synthetic methods.

Acknowledgements

The authors would like to thank the Advanced Microscopy Laboratory and CRANN for access to their facilities. VN wish to acknowledge support

from the European Research Council (ERC Starting Grant 2DNanoCaps, ERC 2D USD), FP7 ITN MoWSeS, the SFI PIYRA and the SFI AMBER Centre.

[1] Smith, R.L., Rohrer, G.S.. Scanning probe microscopy of cleaved molybdates: α-$moo_3(010)$, $mo_{18}o_{52}(100)$, $mo_8o_{23}(010), and\eta$-$mo_4o_{11}(100)$. J Solid State Chem 1996;124(1):104–115.

[2] Wang, S.T., Zhang, Y.G., Ma, X.C., Wang, W.Z., Li, X.B., Zhang, Z.D., et al. Hydrothermal route to single crystalline alpha-moo_3 nanobelts and hierarchical structures. Solid State Commun 2005;136(5):283–287.

[3] Besenhard, J.O., Heydecke, J., Fritz, H.P.. Characteristics of molybdenum oxide and chromium oxide cathodes in primary and secondary organic electrolyte lithium batteries i. morphology, structure and their changes during discharge and cycling. Solid State Ionics 1982;6(3):215–224.

[4] Swiatowska-Mrowiecka, J., de Diesbach, S., Maurice, V., Zanna, S., Klein, L., Briand, E., et al. Li-ion intercalation in thermal oxide thin films of moo_3 as studied by xps, rbs, and nra. J Phys Chem C 2008;112(29):11050–11058.

[5] Mendoza-Sánchez, B., Brousse, T., Ramirez-Castro, C., Nicolosi, V., S. Grant, P.. An investigation of nanostructured thin film α-moo_3 based supercapacitor electrodes in an aqueous electrolyte. Electrochim Acta 2013;91(0):253–260.

[6] Spahr, M.E., Novak, P., Haas, O., Nesper, R.. Electrochemical insertion of lithium, sodium, and magnesium in molybdenum(vi) oxide. J Power Sources 1995;54(2):346–351.

[7] Besenhard, J.O., Heydecke, J., Wudy, E., Fritz, H.P., Foag, W.. Characteristics of molybdenum oxide and chromium oxide cathodes in primary and secondary organic electrolyte lithium batteries. part ii. transport properties. Solid State Ionics 1983;8(1):61–71.

[8] Dickens, P.G., Reynolds, G.J.. Transport and equilibrium properties of some oxide insertion compounds. Solid State Ionics 1981;5(0):331–334.

[9] Riley, L.A., Lee, S.H., Gedvilias, L., Dillon, A.C.. Optimization of moo_3 nanoparticles as negative-electrode material in high-energy lithium ion batteries. J Power Sources 2010;195(2):588–592.

[10] Meduri, P., Clark, E., Kim, J.H., Dayalan, E., Sumanasekera, G.U., Sunkara, M.K.. Moo_{3-x} nanowire arrays as stable and high-capacity anodes for lithium ion batteries. Nano Lett 2012;12(4):1784–1788.

[11] Brezesinski, T., Wang, J., Tolbert, S.H., Dunn, B.. Ordered mesoporous α-moo_3 with iso-oriented nanocrystalline walls for thin-film pseudocapacitors. Nat Mater 2010;9(2):146–151.

[12] Mendoza-Sánchez, B., Grant, P.S.. Charge storage properties of a α-moo_3/carboxyl-functionalized single-walled carbon nanotube composite electrode in a li ion electrolyte. Electrochim Acta 2013;98(0):294–302.

[13] Jung, Y.S., Lee, S., Ahn, D., Dillon, A.C., Lee, S.H.. Electrochemical reactivity of ball-milled moo_{3-y} as anode materials for lithium-ion batteries. J Power Sources 2009;188(1):286–291.

[14] Hassan, M.F., Guo, Z.P., Chen, Z., Liu, H.K.. Carbon-coated moo_3 nanobelts as anode materials for lithium-ion batteries. J Power Sources 2010;195(8):2372–2376.

[15] Butler, S.Z., Hollen, S.M., Cao, L., Cui, Y., Gupta, J.A., Gutirrez, H.R., et al. Progress, challenges, and opportunities in two-dimensional materials beyond graphene. ACS Nano 2013;7(4):2898–2926.

[16] Chhowalla, M., Shin, H.S., Eda, G., Li, L.J., Loh, K.P., Zhang, H.. The chemistry of two-dimensional layered transition metal dichalcogenide nanosheets. Nature Chem 2013;5(4):263–275.

[17] Nicolosi, V., Chhowalla, M., Kanatzidis, M.G., Strano, M.S., Coleman, J.N.. Liquid exfoliation of layered materials. Science 2013;340(6139).

[18] Coleman, J.N., Lotya, M., O'Neill, A., Bergin, S.D., King, P.J., Khan, U., et al. Two-dimensional nanosheets produced by liquid exfoliation of layered materials. Science 2011;331(6017):568–571.

[19] Hughes, J.M., Aherne, D., Coleman, J.N.. Generalizing solubility parameter theory to apply to one- and two-dimensional solutes and to incorporate dipolar interactions. J Appl Polym Sci 2013;127(6):4483–4491.

[20] Cunningham, G., Lotya, M., Cucinotta, C.S., Sanvito, S., Bergin, S.D., Menzel, R., et al. Solvent exfoliation of transition metal dichalcogenides: Dispersibility of exfoliated nanosheets varies only weakly between compounds. ACS Nano 2012;6(4):3468–3480.

[21] Bergin, S.D., Sun, Z., Rickard, D., Streich, P.V., Hamilton, J.P., Coleman, J.N.. Multicomponent solubility parameters for single-walled carbon nanotubesolvent mixtures. ACS Nano 2009;3(8):2340–2350.

[22] Hernandez, Y., Nicolosi, V., Lotya, M., Blighe, F.M., Sun, Z., De, S., et al. High-yield production of graphene by liquid-phase exfoliation of graphite. Nat Nano 2008;3(9):563–568.

[23] Mendoza Sánchez, B., Rasche, B., Nicolosi, V., Grant, P.. Scaleable ultra-thin and high power density graphene electrochemical capacitor electrodes manufactured by aqueous exfoliation and spray deposition. Carbon 2012;52:337–346.

[24] Zhao, X., Mendoza-Sánchez, B., Dobson, P.J., Grant, P.S.. The role of nanomaterials in redox-based supercapacitors for next generation energy storage devices. Nanoscale 2011;3(3):839–855.

[25] Hanlon, D., Backes, C., Higgins, T., Hughes, J.M., O'Neill, A., King, P.J., et al. Production of molybdenum trioxide nanosheets by liquid exfoliation and their application in high performance supercapacitors. Chem Mater 2014;.

[26] Wu, Z., Chen, Z., Du, X., Logan, J.M., Sippel, J., Nikolou,

M., et al. Transparent, conductive carbon nanotube films. Science 2004;305(5688):1273–1276.

[27] Dieterle, M., Weinberg, G., Mestl, G.. Raman spectroscopy of molybdenum oxides part i. structural characterization of oxygen defects in moo_{3-x} by dr uv/vis, raman spectroscopy and x-ray diffraction. Phys Chem Chem Phys 2002;4(5):812–821.

[28] Py, M.A., Maschke, K.. Intra- and interlayer contributions to the lattice vibrations in moo_3. Physica B+C 1981;105(13):370–374.

[29] Mestl, G., Ruiz, P., Delmon, B., Knozinger, H.. Oxygen-exchange properties of moo3: An in situ raman spectroscopy study. J Phys Chem 1994;98(44):11269–11275.

[30] Scanlon, D.O., Watson, G.W., Payne, D.J., Atkinson, G.R., Egdell, R.G., Law, D.S.L.. Theoretical and experimental study of the electronic structures of moo_3 and moo_2. J Phys Chem C 2010;114(10):4636–4645.

[31] Tsumura, T., Inagaki, M.. Lithium insertion/extraction reaction on crystalline moo_3. Solid State Ionics 1997;104(3-4):183–189.

[32] Iriyama, Y., Abe, T., Inaba, M., Ogumi, Z.. Transmission electron microscopy (tem) analysis of two-phase reaction in electrochemical lithium insertion within -moo3. Solid State Ionics 2000;135(1-4):95–100.

[33] Zhao, X., Johnston, C., Grant, P.S.. A novel hybrid supercapacitor with a carbon nanotube cathode and an iron oxide/carbon nanotube composite anode. J Mater Chem 2009;19(46):8755–8760.

[34] Zhao, X., Johnston, C., Crossley, A., Grant, P.S.. Printable magnetite and pyrrole treated magnetite based electrodes for supercapacitors. J Mater Chem 2010;20(36):7637–7644.

[35] Qu, Q., Zhang, P., Wang, B., Chen, Y., Tian, S., Wu, Y., et al. Electrochemical performance of mno_2 nanorods in neutral aqueous electrolytes as a cathode for asymmetric supercapacitors. J Phys Chem C 2009;113(31):14020–14027.

[36] Huang, Q., Wang, X., Li, J.. Characterization and performance of hydrous manganese oxide prepared by electrochemical method and its application for supercapacitors. Electrochim Acta 2006;52(4):1758–1762.